RESEARCH ARTICLE

VOLCANICA

Subglacial volcano monitoring with fiber-optic sensing: Grímsvötn, Iceland

Sara Klaasen*[α], Solvi Thrastarson[α], Yeşim Çubuk-Sabuncu[β], Kristín Jónsdóttir[β], Lars Gebraad[α], Patrick Paitz[α], and Andreas Fichtner[α]

[α] ETH Zürich, Institute of Geophysics, Zürich, Switzerland.
[β] Veðurstofa Íslands (Icelandic Meteorological Office), Reykjavík, Iceland.

Submitted: 2023-05-09 | Accepted: 2023-07-02 | Published: 2023-09-05

Editor: B. Kennedy | Typesetter: E. Hughes

Abstract

We present a distributed acoustic sensing (DAS) experiment at Grímsvötn, Iceland. This is intended to investigate volcano-microseismicity at Grímsvötn specifically, and to assess the suitability of DAS as a subglacial volcano monitoring tool in general. In spring 2021, we trenched a 12 km long fiber-optic cable into the ice sheet around and within the caldera, followed by nearly one month of continuous recording. An image processing algorithm that exploits spatial coherence in DAS data detects on average ~100 events per day, almost 2 orders of magnitude more than in the regional earthquake catalog. A nonlinear Bayesian inversion reveals the presence of pronounced seismicity clusters, containing events with magnitudes between −3.4 and 1.7. Their close proximity to surface volcanic features suggests a geothermal origin. In addition to painting a fine-scale picture of seismic activity at Grímsvötn, this work confirms the potential of DAS in subglacial volcano monitoring.

Keywords: Distributed acoustic sensing; Volcano monitoring; Subglacial volcano; Hamiltonian Monte Carlo inversion; Magnitudes; Earthquakes.

1 Introduction

Detailed seismic monitoring of subglacial volcanoes is often hindered by their location in remote and hazardous environments, where challenging accessibility prohibits the installation and maintenance of dense, conventional seismic networks. Under such conditions, emerging fiber-optic sensing technologies may be an attractive alternative, thanks to their high spatio-temporal sampling. This large data volume, combined with the robustness of the fibers and their low footprint in deployment and maintenance, leads to the potential of DAS as a volcano monitoring tool.

Within the growing family of fiber-optic sensing approaches, Distributed Acoustic Sensing (DAS) of ground deformation along a cable has received particular attention in the geosciences [e.g. Lindsey and Martin 2021]. DAS provides a network of measurements with meter-scale resolution that can extend up to several tens of kilometers length, with a sampling rate in the kHz range [Hartog 2017]. The density of this network, combined with the broadband instrument response [Jousset et al. 2018; Lindsey et al. 2020; Paitz et al. 2021], have led to a wide range of applications, for instance, in active and passive near-surface imaging and monitoring [e.g. Daley et al. 2013; Mateeva et al. 2014; Daley et al. 2016; Dou et al. 2017; Martin et al. 2017], earthquake wavefield observations [Lindsey et al. 2017; Wang et al. 2018; Ajo-Franklin et al. 2019], and glaciology [e.g. Walter et al. 2020; Hudson et al. 2021; Fichtner et al. 2023]. A series of recent DAS studies on volcanoes without a large ice cover [e.g. Currenti et al. 2021; Klaasen et al. 2021; Fichtner et al. 2022; Flóvenz et al. 2022; Jousset et al. 2022; Thelen et al. 2022] suggest that the technology may equally contribute to subglacial volcano monitoring.

* sara.klaasen@erdw.ethz.ch

Grímsvötn in Iceland is a prominent example of a major subglacial volcanic system and a comparatively convenient testing ground for fiber-optic seismology. Located above the Iceland hotspot and underneath the Vatnajökull ice cap, it produced one of the largest basaltic lava flows in human historic times; the Laki (Skaftár Fires) eruption from 1783–1784 [Thordarson and Self 1993], which had extensive atmospheric and environmental effects [Thordarson and Self 2003]. A low-velocity body underneath Grímsvötn suggests that its magma chamber extends to ~3 km below the surface and is flanked by higher-velocity anomalies underneath the caldera rim [Alfaro et al. 2007]. Additionally, gravity data indicates the existence of a more extended magma chamber to depths between 1.5–4 km [Guðmundsson and Milsom 1997]. This environment leads to geothermal activity that melts the glacier from below, and sustains a semi-stable subglacial lake within the central caldera [Björnsson and Guðmundsson 1993]. Figure 1 shows the setting of Grímsvötn, including the approximate locations of its most recent eruptions.

Grímsvötn is Iceland's most active volcano, with more than 70 eruptions occurring in the last 1000 years. Its most recent major eruption in 2011 included several ash plumes reaching altitudes up to 15–20 km [Global Volcanism Program 2011]. The area is prone to quasi-periodic jökulhlaups, as the subglacial lake fills with glacial meltwater until its ice dam breaches and the lake drains [Reynolds et al. 2018]. Both the ash clouds and the jökulhlaups form the largest hazards of Grímsvötn, which can severely affect infrastructure, agriculture, and aviation.

The broad range of Grímsvötn's natural hazards demands continuous monitoring and improvements of early-warning systems that prolong warning times as much as possible. Experience with Hekla volcano in Iceland has shown that the densification of seismic stations can increase warning times

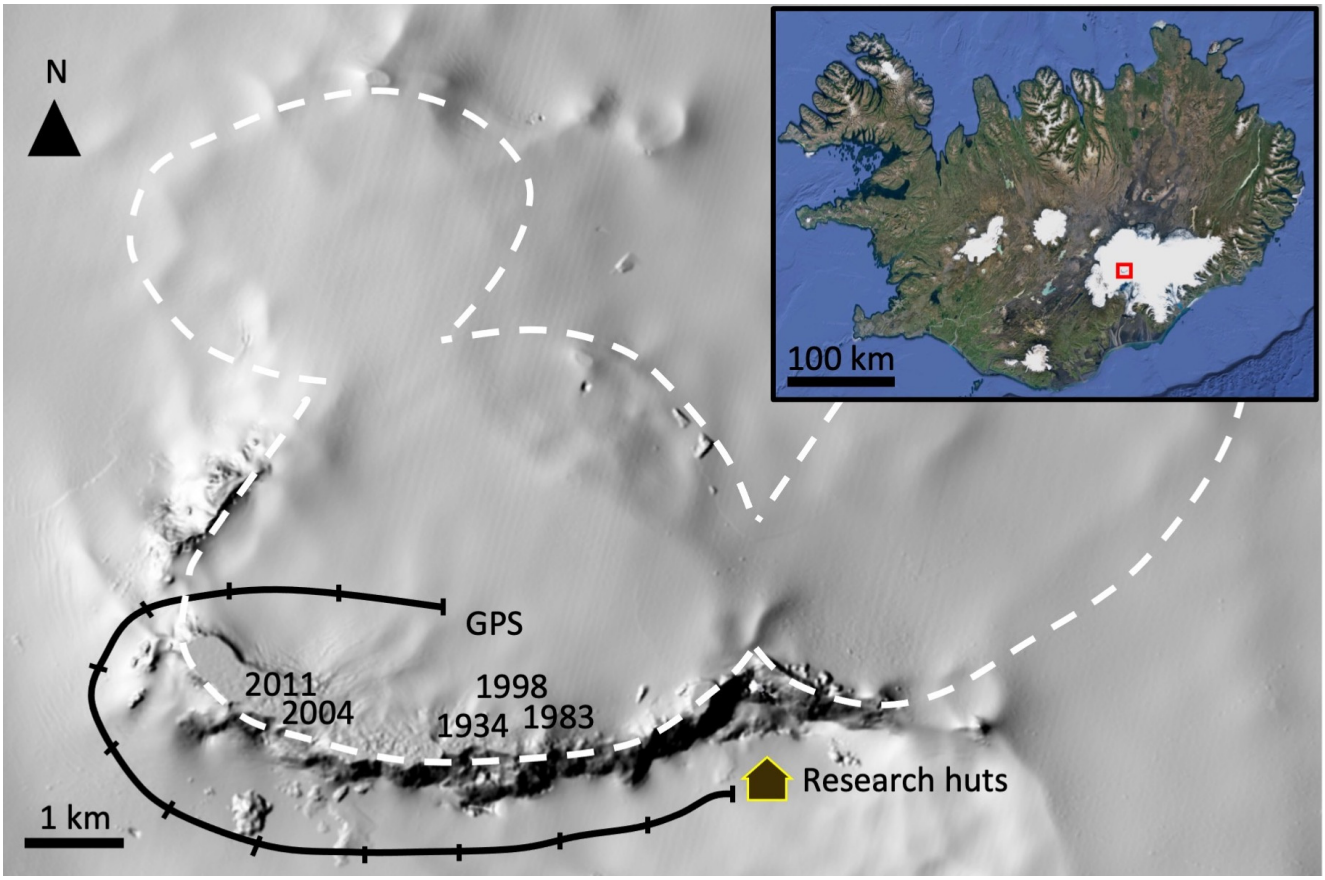

Figure 1: The ~12 km long DAS cable extends along the caldera rim and onto the subglacial lake on top of Grímsvötn. The DAS interrogator and a seismometer were located at the research huts, while a GPS sensor was placed near the end of the cable above the subglacial lake. The year numbers indicate approximate locations of previous fissure eruptions [Hreinsdotóttir et al. 2014], the dashed white line demarcates the caldera boundary, and the inset shows the location of Grímsvötn in Iceland. (Sources: topography Porter et al. 2018, inset [Imagery ©2023 TerraMetrics, Map data ©2023]).

from ~30 minutes to nearly 2 hours [Barsotti et al. 2019]. At Grímsvötn, however, the challenging environment complicates the installation and maintenance of extensive conventional seismic networks. Here, we investigate whether DAS can be an alternative monitoring option, because its operation requires comparatively low labor and financial costs.

This research focuses on the experimental logistics, the development of methods and codes for automated event detection and location, and the exploration of our specific dataset. The paper is structured around the following themes: 1) fieldwork logistics, 2) seismic event detection using image processing techniques, 3) arrival time estimation based on cross correlations, and 4) event location by probabilistic inversion that jointly constrains event locations and velocity structure.

2 Experimental setup and logistics

We collected the seismological data in spring 2021, which resulted in approximately one month of continuous recordings [Klaasen et al. 2022]. The installation of the ~12 km long Solifos BRUfield fiber-optic cable took 3 days, including trenching the cable ~50 cm into the ice with a custom-made ice plough pulled behind a snowcat, splicing parts of the cable, and performing tap tests every 200 m along the cable in order to link DAS channels to their geographic locations. Figure 1 shows the layout of the fiber-optic cable along the caldera. The area experienced more snowfall after the deployment, which ensured that the cable was frozen into the ice and well protected against wind and temperature fluctuations.

We used a Silixa iDAS v2 interrogator that ran continuously on power from a generator and batteries from 13–14 April 2021 and from 6–28 May 2021, with a sampling rate of 200 Hz, a channel spacing of 8 m, and a gauge length of 10 m. These parameters strike a reasonable balance between limiting the data volume and recording high-resolution signals of local seismicity. The total data volume amounts to 1.35 TB. Using only snow scooters, a team from the Icelandic Meteorological Office (IMO) was able to retrieve the cable, primarily for environmental reasons, during one day in August 2021, when the snow overlying the cable had melted away. More technical details concerning the experimental setup and a video* with an impression of the fieldwork are given in Supplementary Material 1 and Klaasen [2023].

*https://youtu.be/J7cxVZvgyWQ

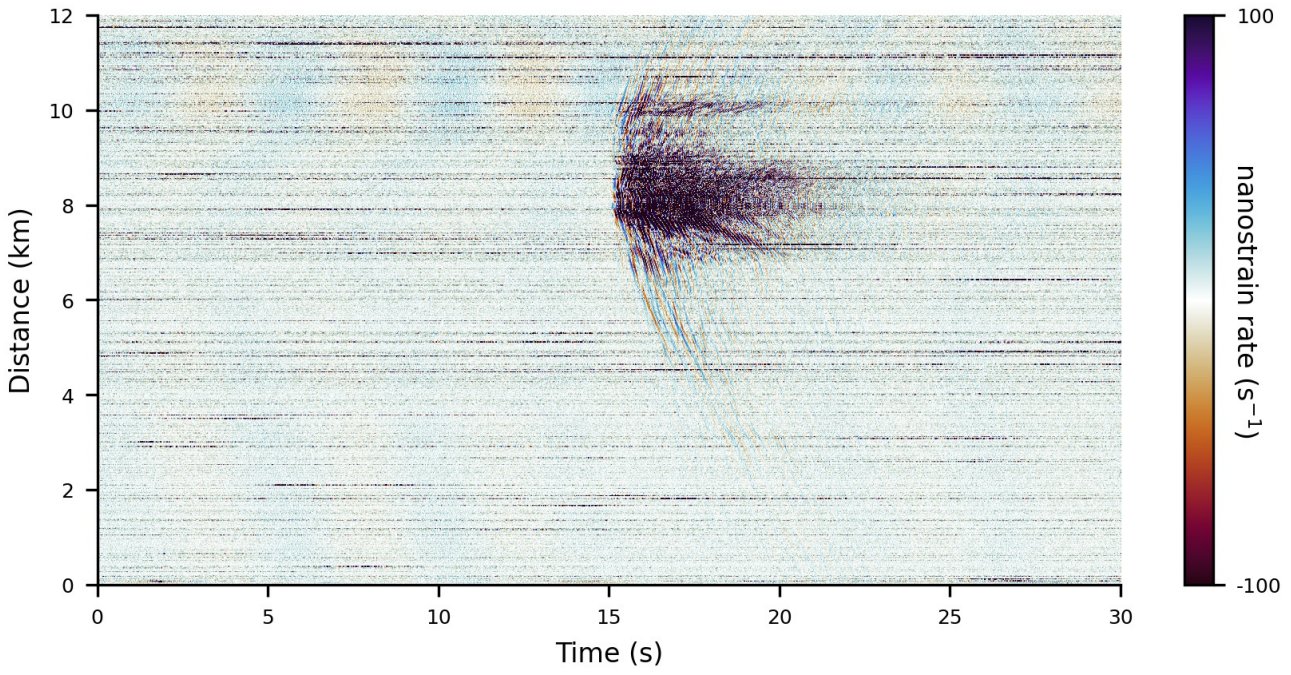

Figure 2: This is an example of a waveform in the raw data (the colorbar is clipped), which is visually distinct from the optical noise. Between kilometers ~9 and ~11.5 along the cable, ice sheet resonance with a dominant frequency of 0.22 Hz is visible, which is present throughout the data [Fichtner et al. 2022]. The location of this quake is marked in Figure 5 and the local magnitude of this event is −0.91.

3 Event detection

The advantageous coupling conditions of the cable led to a dataset of unexpectedly high quality. Without the need for any preprocessing, we can identify numerous quakes recorded along parts of the cable. A representative example is shown in Figure 2, superimposed onto low-amplitude background oscillations near the end of the cable, which are caused by resonance of the ice sheet floating on top of the subglacial lake [Fichtner et al. 2022]. The coherent observability of these oscillations throughout the one-month experiment illustrates that strain rate amplitudes in the range of 10 nanostrain s^{-1} could be reliably recorded. Optical noise from the interrogator appears as horizontal stripes in Figure 2, as it tends to affect single channels for some period of time, typically several seconds.

While transient events are easily visible in the data without processing, the size of the data volume prohibits the manual compilation of an earthquake catalog, thereby requiring an automated approach. Single-trace detection methods [e.g. Allen 1978; Sleeman and van Eck 1999; Saragiotis et al. 2002], while being mature and well-understood, are by design unable to capitalize on the spatial coherence of seismic event recordings offered by DAS. Algorithms based on artificial neural networks [e.g. Gentili and Michelini 2006; Zhu and Beroza 2019] have the added disadvantage of requiring a sufficiently large training dataset, which is not available for Grímsvötn.

To exploit spatial coherence for event detection and travel-time estimation, we implement and adapt an algorithm based on a sequence of image processing techniques, the details of which are described in Thrastarson et al. [2021]. Here we limit ourselves to a condensed summary. The algorithm starts with standard pre-processing steps, such as detrending and bandpass filtering. Subsequently, every data point in time and space is treated as the pixel of an image. Each pixel is then transformed to binary ('True' or 'False') based on the intensity of the amplitudes. We then select and remove all clusters of 'True' points that form a purely horizontal line, as visible in Figure 2, as their 'True' values are caused by optical noise. We also eliminate data points that form small clusters of 'True' values that only affect few channels for a short period of time. Finally, we retain signals that are coherent in space and time, with True values in larger clusters.

The output of the algorithm is a catalog with an approximate recording window in time and space for each event. In total, we detect 1828 events during the entire acquisition period. This corresponds to around 50–150 events per day, normalized for the recorded time per day, see Figure 3. This level of seismicity is significantly higher than previously known. In fact, only ~1.3 % of these events can be found in the catalog of the IMO, based on data from the South Iceland Lowland (SIL) network.

4 Arrival time estimation

To locate the detected events, we require arrival time measurements along the cable. An algorithm for automated arrival time estimation in DAS recordings should harness the spatial coherence, while being able to handle variable signal-

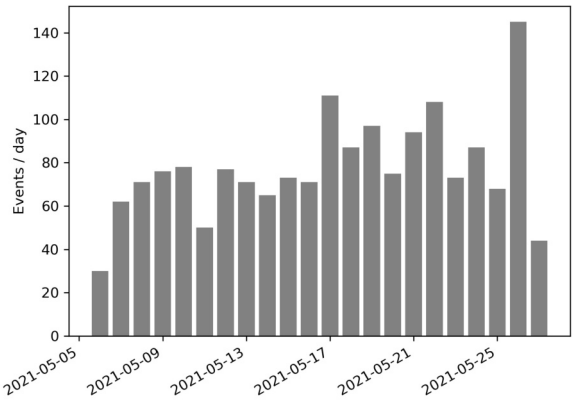

Figure 3: The number of events recorded per day with DAS reveals 50–150 events per day. The first and last day of recordings contain less events as we did not record for the full day.

to-noise ratios (SNR), large data volumes, as well as emerging (non-impulsive) onsets that are typical for the Grímsvötn data.

To achieve these goals, we propose a fully automated algorithm based on inter-channel cross-correlations. It exploits spatial coherence while having only weak dependence on absolute amplitudes. Figure 4 illustrates the different steps of the algorithm.

Prior to the arrival time estimation, only the approximate space time window of an event, as obtained from the detection algorithm, is available. A typical example is shown in Figure 4A. The first step is the determination of the SNR of each individual channel, using a noise window of 2 s prior to the event. Subsequently, we cross-correlate all channels with an SNR above a threshold with their nearest neighbours. During this cross-correlation, we measure the full width at half maximum (FWHM) of the correlation peak, and use it as a conservative arrival time error in the later event location. For the channels with an SNR below the threshold, we linearly interpolate the time shifts and their errors from the surrounding channels where the SNR is above the threshold. The result of this procedure is a pattern of relative arrival times. To obtain absolute arrival times, we correlate the arrival times with the data and determine the best-matching absolute time. The result, for our example, is shown in Figure 4B.

To refine the arrival time estimates, we define a time window around these initial estimates, shown with the dashed gray lines in Figure 4C. We then repeat the previous steps of cross-correlation, interpolation and the correlation of the relative arrival-time pattern with the data using only the data within the time window. The repetition of these steps with sequentially shortened time windows in Figure 4C–E ensures that the absolute arrival time estimates converge towards the first-arrival times in the data, rather than later phases. The final result, shown in Figure 4E, is repeated in greater detail in Figure 4F.

The SNR threshold, allowed correlation shift, exact number of iterations, and the definition of time windows during each iteration are the most important tuning parameters of the algorithm. We determine useful values for them by trial and error for a few events, such that the resulting approximate arrival time estimates seem to fit the data. We use an SNR threshold for each event of 1.5 during the first iteration, and 1.1 during the later iterations. The allowed correlation shift changes per channel pair, and is determined by the physical distance between the channels and an assumed minimum velocity of $600\,\mathrm{m\,s^{-1}}$.

The result is a catalog of the first arrival time estimates and their errors for 1803 events. The arrival times of the remaining 25 events could not be constrained, since they were recorded at an insufficient number of channels with an SNR above the threshold.

5 Event location

The location of events based on DAS data from areas with complex geology suffers from three related classes of difficulties. (1) The seismic velocity structure is poorly known. In the special case of Grímsvötn, this problem is further exacerbated by rough topography, the ice cover and the presence of the subglacial lake, all of which change geometry significantly on time scales of days to weeks. (2) Seismic phases may not be unambiguously identified. This issue is caused by the complex geology but also the unidirectionality of DAS recordings, which precludes phase identification by polarization analysis. In our data, some of the first observable waves may, for instance, be Rayleigh waves and not lower-amplitude P- or S-waves that may be below the noise level. (3) The combination of (1) and (2) leads to a nonlinear inverse problem, where event location and phase-specific velocity structure must be constrained jointly. Hence, the application of linearized inversion procedures is excluded.

In the absence of a detailed velocity and geometry model for Grímsvötn, the joint inversion for 1803 event locations and a fully 3-D velocity model from scratch is clearly out of scale. Therefore, we adopt a simplified approach, which provides useful estimates that may later be refined with the help of full-waveform modelling and inversion techniques. Specifically, we model the arrival time τ of an event as

$$\tau = \frac{||\mathbf{x}_{\mathrm{station}} - \mathbf{x}_{\mathrm{event}}||}{v_{\mathrm{effective}}} + \tau_0\,, \tag{1}$$

with the unknown event location $\mathbf{x}_{\mathrm{event}}$, the position of a DAS channel $\mathbf{x}_{\mathrm{station}}$, and the origin time τ_0. The effective seismic velocity $v_{\mathrm{effective}}$ is considered constant for each event, and it depends on both the *a priori* unknown nature of the seismic phase and the propagation paths in the region between source and the DAS channels where the event was recorded. Hence, for each event, the model parameter vector is given by $\mathbf{m} = [\mathbf{x}_{\mathrm{event}}, v_{\mathrm{effective}}, \tau_0]^T$.

To properly account for the nonlinearity and trade-offs between the model parameters, we employ the Hamiltonian Monte Carlo (HMC) algorithm. Originally developed for quantum chromodynamics simulations [Duane et al. 1987], HMC can serve as a Bayesian inference tool that largely derives its efficiency from the use of gradient information [e.g. Neal 2012; Betancourt 2017]. Recently, HMC has been adapted to seismic

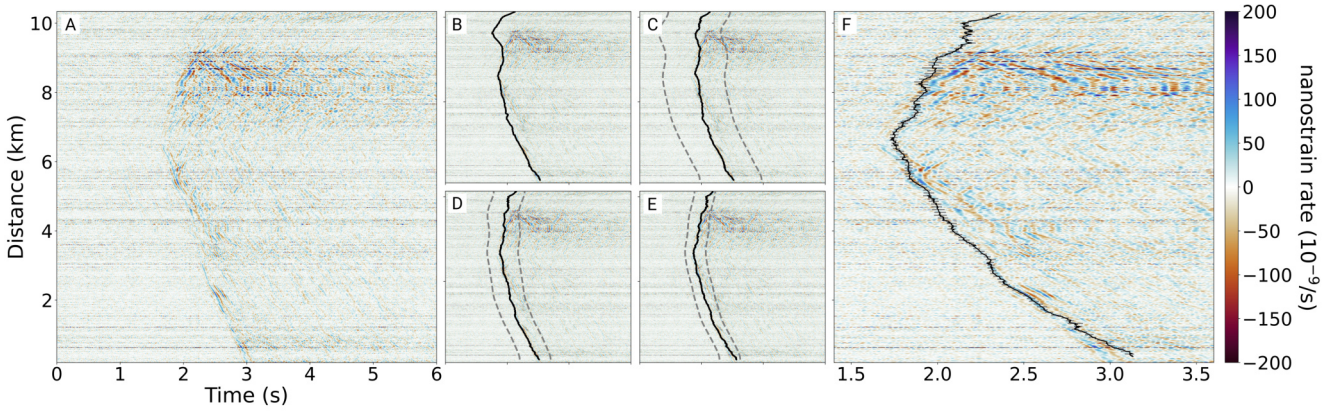

Figure 4: The arrival time estimates are refined in four iterations [B, C, D, E] with the following steps: [A] approximate space-time window of the event, [B] the initial arrival times based on the waveforms of the entire event, [C], [D], [E] refinement of the arrival time estimates using the data window given by the dashed gray line only, and [F] a zoom into the final result with error bars every 10th channel for visibility. The location of this quake is marked in Figure 5 and the local magnitude of this event is 0.56.

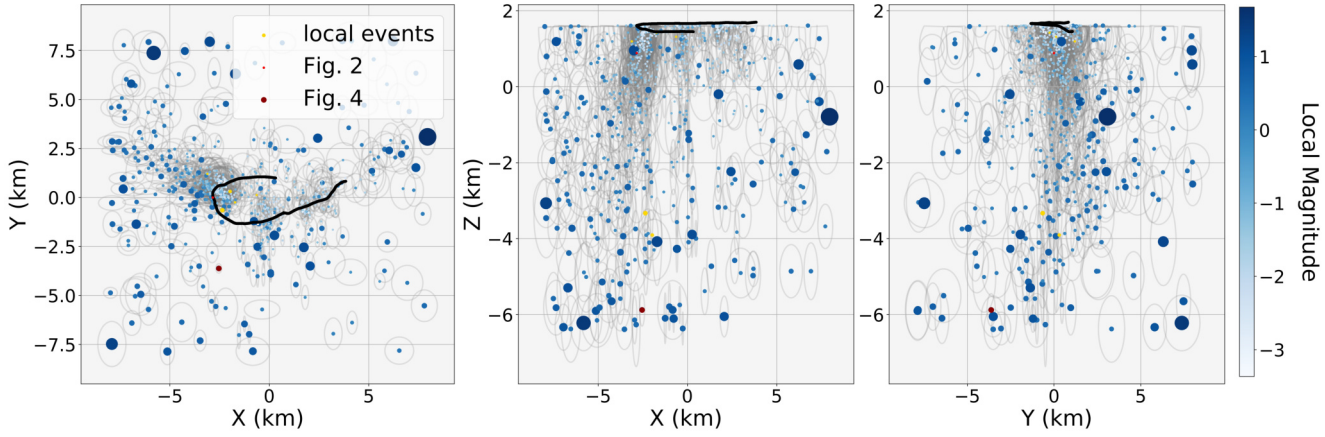

Figure 5: The locations of 726 events in the vicinity of the fiber-optic cable reveal clusters in seismicity. Gray ellipses indicate the standard deviation of the location error. The size and shading of the dots correspond to the local magnitude of each event. Events marked in yellow were recorded by our DAS network and are also present in the national catalog of IMO.

event characterization [e.g. Fichtner and Simute 2018; Masfara et al. 2022; Simute et al. 2023].

Within the Bayesian inference framework, we assume approximately Gaussian error statistics and define the data space prior, or the likelihood function, as

$$p(\tau_{\text{obs}}|\mathbf{m}) \propto \exp\left[-\frac{1}{2}\sum_{i=1}^{N}\left(\frac{\tau^i_{\text{obs}} - \tau^i_{\text{calc}}(\mathbf{m})}{\sigma_i}\right)^2\right], \quad (2)$$

where the summation is over the squared difference between the N observed arrival times τ^i_{obs} and the calculated arrival times $\tau^i_{\text{calc}}(\mathbf{m})$. The scaling σ_i is the observational error standard deviation estimated in the arrival time measurement procedure described above. For the prior distribution in model space, $p(\mathbf{m})$, we use a uniform distribution between 10 and 10 000 m s^{-1} for the effective velocity, with a starting model of 1200 m s^{-1}. We choose the least informative velocity prior to ensure no preference is given for any medium the waves can travel through, such as the bedrock, ice, snow, water, or air (due to topography). For the event location, we define a uniform prior distribution that is centered around the mean coordinate of the DAS channels and extends 16 km in both horizontal directions and 8 km below the surface. The two priors are chosen conservatively and combined into the posterior distribution using Bayes' theorem, $p(\mathbf{m}|\tau_{\text{obs}}) \propto p(\tau_{\text{obs}}|\mathbf{m})p(\mathbf{m})$ [e.g. Bayes 1763; Tarantola 2005; Fichtner 2021]. For the practical implementation of HMC, we use the freely available `HMCLab` code package [Zunino et al. 2023].

We initially attempt to constrain the location of all events for which we estimated arrival times. Subsequently, we exclude events with a location uncertainty exceeding the picking uncertainty or a location uncertainty above 1500 m, which typically results from the absence of a clearly defined maximum in the posterior distribution. The maximum-likelihood locations plus standard deviations of the remaining 726 events are displayed in Figure 5. The resulting effective velocities of the events range from 435 to 8477 m s^{-1}. The procedure for magnitude estimation will be described in the following section.

6 Event magnitude

To enable comparisons with local earthquake magnitudes (Ml) computed by IMO, we adopt their methodology to estimate the local magnitudes of all the events detected and located with our DAS data. The IMO procedure was originally developed for the SIL network, which started in 1988 to investigate earthquakes in the South Iceland seismic zone with automated earthquake analyses [Slunga 1981; Stefánsson et al. 1993; Böðvarsson et al. 1996; Böðvarsson and Lund 2003]. This network utilizes data from a few seismic stations near Grímsvötn, with 1 station located near the huts, and 4 other stations within a radius of 30 km around the cable. Though their procedure is similar to standard observatory approaches to magnitude estimation, the application of the method to DAS data is nontrivial because it is based on displacement velocity and not on unidirectional strain rate. Hence, a conversion from strain rate to displacement is often a prerequisite to derive information about event magnitudes from DAS data [Lellouch et al. 2020; Lior et al. 2021].

The magnitude estimation starts with a high-pass filter with a 1.5 Hz cut-off frequency, which eliminates lower-frequency noise that may corrupt the subsequent integration from the strain rate to strain. As explained in detail by Paitz et al. [2021], strain can be converted to velocity using the relation

$$\epsilon(\mathbf{x}, t) \approx \frac{1}{c(\mathbf{x}, t)} v(\mathbf{x}, t)\,, \tag{3}$$

where ϵ is the strain measured in the direction of the cable, c is the apparent phase velocity along the local cable direction, and v is the displacement velocity in the direction of the cable, that is, the time derivative of the particle displacement in $\mathrm{m\,s^{-1}}$. All these quantities depend on the position along the cable $\mathbf{x}$ and time t. Equation 3 uses the plane-wave approximation. The effective velocity is one of the outcomes of the HMC algorithm, which yields one distinct velocity for each event. However, this velocity corresponds to the waves of the first arrival times, whereas the magnitude estimation is based on the waves with the largest amplitudes, irrespective of their phase. Therefore, we rescale the effective velocity for each channel to correspond to the velocity of the waves with the largest amplitudes. This results in a distinct scaling velocity for every channel, which we use to convert the data from strain to displacement velocity.

The SIL magnitude estimation is based on counts, which are related to displacement velocity by

$$\text{counts} = \alpha\, v\,, \tag{4}$$

where several constants, unknown for DAS, are combined in the α term. We approximate this scalar conversion by calibrating our results with the events recorded by both the regional seismometer and our DAS network. The local magnitude for the i^{th} station in the network is defined as

$$m_i = \log_{10}(A_i) + 2.1 \log_{10}(D_i) - 4.8\,, \tag{5}$$

where A_i is the maximum peak to peak amplitude in counts, and D_i is the distance between the station and the event in km. Finally, we obtain the local magnitude m of the event by averaging over all m_i that fall within ± 0.5 of their median.

The combined effect of integrating the data, the velocity conversion, the count calibration and the assumed proximity of all events, leads to a local magnitude scale that has to be interpreted with some care. The results are summarized in Figure 6A, which shows the cumulative magnitude distribution on a Gutenberg-Richter plot [Gutenberg 1956] that reveals a plausible b-value around 1.5. The derived catalog with earthquake detections, locations, and magnitudes is given in Supplementary Material 2.

7 Discussion

Our results underline the potentials and challenges of DAS on subglacial volcanoes. While this pilot experiment provides new insights into the Grímsvötn volcanic system, it also suggests improvements that could further develop DAS as a volcano-monitoring tool.

Despite initial doubts concerning the feasibility of such an experiment, the logistics were unexpectedly successful, resulting in a well-coupled cable and a rich dataset of high quality. Based on the experience that we gained, the logistic effort of future experiments may be reduced significantly. For example, we employed a snowcat to trench the fiber-optic cable into the ice, but discovered during the experiment that this may also have been achieved with a light snow scooter. Another consideration for experiments with longer duration would be to avoid areas with rapid glacial flows, as this may damage the cable. We recorded very noisy data towards the end of the acquisition period near the steepest section of the cable, which may be related to the onset of cable failure.

The large number of detected events exceeded our prior expectations, as the national network does not record this level of seismicity. This emphasizes the lower detection threshold of DAS, which reveals microseismicity at magnitudes down to around -3. The majority of these events are local as they are recorded only on small sections of the cable with emergent onsets. This is in contrast to the few larger events recorded on the entire cable with distinct P- and S-wave arrivals. The largest recorded earthquake is the M7.3 earthquake from Southern Qinghai, China, on 21 May 2021. We did not observe any obvious temporal systematics in the event detections, as shown in Figure 3, which may require longer acquisition periods.

The earthquake locations reveal three pronounced clusters of shallow microseismicity, emphasized in Figure 7A. Major cauldrons and fumaroles can be found within or near all of the clusters. Though a glacial origin of these events cannot be excluded, their spatial association to volcanic features at the surface suggests a geothermal origin. A definite identification of the underlying mechanisms would require a more precise event depth estimation, possibly combined with a moment tensor inversion. A more detailed structural model would, however, be a prerequisite for this refinement. Figure 7B shows the reviewed earthquake catalog of IMO for a period of 30 years (1991–2021) at Grímsvötn. While it reveals a large collection of earthquakes, it notably lacks quakes in cluster 1 that we record with DAS. The catalog of IMO has a detection

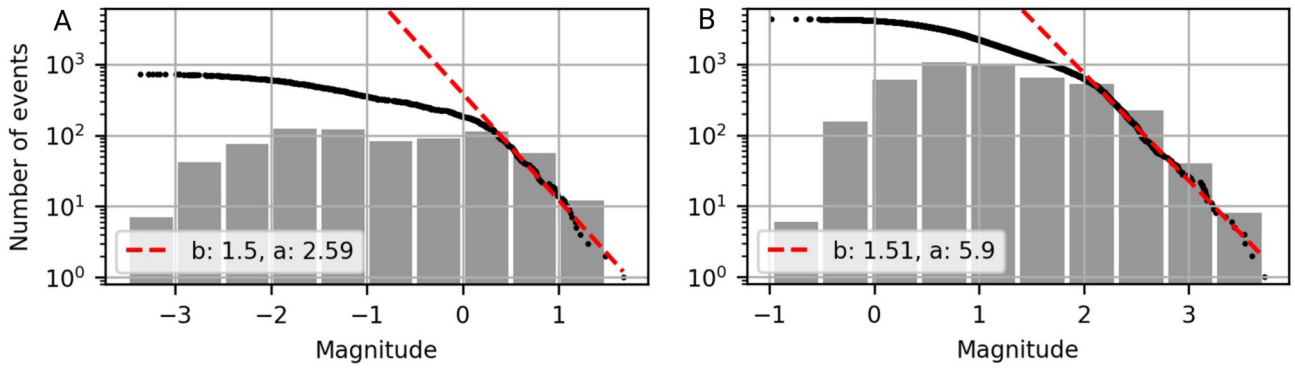

Figure 6: [A] The Gutenberg-Richter distribution of all events from DAS reveals a b-value near 1.5 over a range of magnitudes between −3.4 and 1.7. [B] The distribution of all reviewed events from IMO of 30 years reveals a similar b-value, and a higher magnitude of completion. The magnitudes are plotted both cumulatively (black dots) and in bins (in gray), while the red dashed line is fitted through the tail of the cumulative distribution.

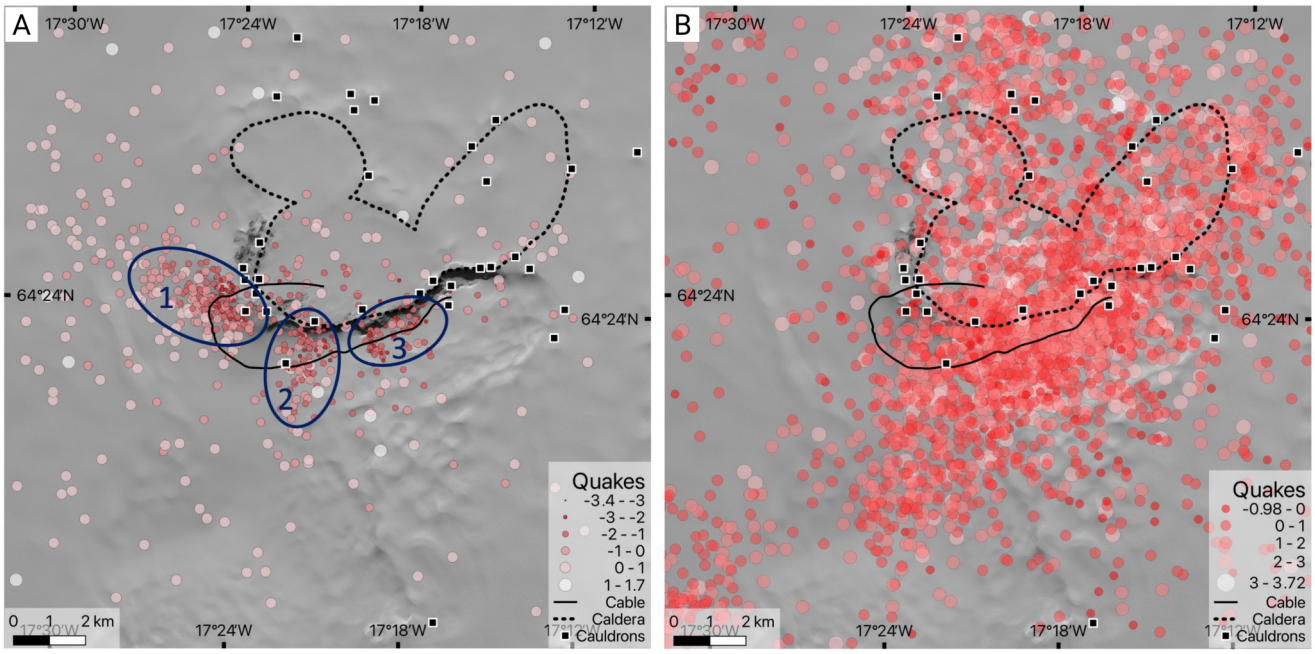

Figure 7: [A] The distribution of earthquake locations from DAS reveals the presence of three pronounced clusters, marked by dark blue ellipses. Major cauldrons, indicated by black squares, can be found near these clusters. Though a glacial origin of these clustered events cannot be excluded, this correlation hints at a geothermal origin. [B] The earthquake catalog from IMO of 30 years at Grímsvötn shows a collection of earthquakes extending in the SW-NE direction, which overlaps with cluster 2 and 3 in A. It does not contain a cluster of quakes that would correspond to cluster 1 in A. (Sources: Landsat-8 image courtesy of the U.S. Geological Survey, cauldron locations are provided by the University of Iceland, and earthquakes in b) are provided by IMO.)

threshold of −2, and a higher magnitude of completion than this DAS dataset, see Figure 6. Consequently, the small events in cluster 1 (e.g. the event in Figure 2) may have been missed by the national network.

The magnitudes of the local earthquakes range from around −3.4 to 1.7, with an elevated b-value of 1.5, which is typical for volcanic environments [Roberts et al. 2015]. Figure 6 shows that this b-value is comparable to the b-value of the catalog of reviewed events of IMO between 1991–2021 in the same area, even though this value is higher than found in previous studies [Got et al. 2017]. We are able to record this level of microseismicity, with a lower detection threshold and magnitude of completeness, thanks to both the good cable coupling and the proximity of the cable to the hypocenters. The ability to deploy a fiber-optic cable near such seismically active and hazardous regions is one of the major advantages of DAS for volcano monitoring.

The methods that we developed in this study focus on utilizing the strengths of DAS data and going towards on-the-fly computing. Whereas the large volume of DAS data and the possibly lower SNR of individual channels may complicate the use of single-trace methods, the dense spatial sampling of DAS

reveals information that can be exploited as well. For longer-term experiments machine-learning methods may prove useful, assuming that a useful training dataset can be compiled. The developed methods have the additional benefit of low computational cost and full automation, which is a necessity to move towards on-the-fly data analysis. This would enable DAS to become an operational volcano-monitoring tool, as it will allow data analysis without the need for extensive storage.

Based on our results, inferences on the seismicity and subsurface structure of Grímsvötn could be further refined through the use of full-waveform modelling and inversion methods [e.g. Komatitsch and Vilotte 1998; Fichtner 2010; Igel 2016] that overcome some of our limiting assumptions, such as one effective velocity per event and the straight ray approximation. This research focuses on the initial data analysis to obtain a first glimpse of the fine-scale seismicity of Grímsvötn with little prior information.

8 Conclusions

From a logistical perspective, the major conclusions of this work are (1) the feasibility of a large-scale fiber-optic sensing experiment on a remote subglacial volcano, and (2) the high data quality, with deformation recorded at the 10 nanostrain s^{-1} level.

This data quality combined with the proximity of the cable to event hypocenters enables the detection of local seismicity with magnitudes as low as −3.4, that is largely being missed by the regional seismometer network. Many of the events fall into a small number of pronounced spatial clusters, typically located in the vicinity of surface volcanic features.

The low detection threshold of DAS may be one of its main advantages for subglacial volcano monitoring. This study aims to provide a basis for systematic future efforts in that direction.

Author Contributions

SK, AF, ST, and KJ contributed to the conceptualization of this paper. SK, ST, YCS, KJ, and AF worked on acquiring the data. SK, ST, and LG worked on the methodology, and SK applied the formal analysis, as well as the writing of the original draft. All authors reviewed the final manuscript.

Acknowledgements

The authors gratefully acknowledge phenomenal support from Silixa throughout all stages of this experiment. Invaluable advice on the selection of a suitable cable was provided by Andrea Fasciati at Solifos AG. This work was partially funded by the Realtime Earthquake Risk Reduction for a Resilient Europe project (RISE) under the European Unions Horizon 2020 research and innovation programme (Grant Agreement Number 821115), and the IS-TREMOR IRF-grant (Grant Agreement Number 217738). We thank JÖRFÍ and Neyðarlínan for access to the huts on Grímsfjall and the power generator. We acknowledge the Institute of Earth Sciences of the University of Iceland for the location of the ice cauldrons, and Ragnar Heiðar Þrastarson for his support to create Figure 7. We also thank everyone who has been involved with the fieldwork: Bergur H. Bergsson, Vilhjálmur Kjartansson, Vala Hjörleifsdóttir, Bergur Einarsson, Laufey Guðmundsdóttir, Guðlaugur Jakob Þorsteinsson, Hlynur Skagfjörð, Jóhannes Rögnvaldsson, Hildur Jónsdóttir, Snæbjörn Sveinsson, Nadine Widmer, and André Blanchard.

Data Availability

Due to the data volume used in our analysis, the data will be made available upon reasonable request to the authors. The earthquake catalogue of IMO used in Figure 6B and Figure 7B is available at `https://skjalftalisa.vedur.is/#/page/map`. The codes used in this work, together with data samples, are freely available in several repositories. Event detection: `https://github.com/solvithrastar/DAS_Auto`, arrival time picking: `https://github.com/saraklaasen/arrival_time_picking`, HMC inversion: `https://hmclab.science`. Additional Supplementary Material is available alongside the online version of this article and in Klaasen [2023] (doi: `10.5281/ZENODO.8318425`).

Copyright notice

References

Ajo-Franklin, J. B., S. Dou, N. J. Lindsey, I. Monga, C. Tracy, M. Robertson, V. Rodriguez Tribaldos, C. Ulrich, B. Freifeld, T. Daley, et al. (2019). "Distributed acoustic sensing using dark fiber for near-surface characterization and broadband seismic event detection". *Scientific Reports* 9. 1328. DOI: `10.1038/s41598-018-36675-8`.

Alfaro, R., B. Brandsdóttir, D. P. Rowlands, R. S. White, and M. T. Guðmundsson (2007). "Structure of the Grímsvötn central volcano under the Vatnajökull icecap, Iceland". *Geophysical Journal International* 168(2), pages 863–876. DOI: `10.1111/j.1365-246X.2006.03238.x`.

Allen, R. V. (1978). "Automatic earthquake recognition and timing from single traces". *Bulletin of the Seismological Society of America* 68 (5), pages 1521–1532. DOI: `10.1785/BSSA0680051521`.

Barsotti, S., M. M. Parks, M. A. Pfeffer, M. J. Roberts, Ófeigsson, G. B. Guðmundsson, K. Jónsdóttir, K. S. Vogfjörð, I. Kristinsson, B. H. Bergsson, and R. H. Þrastarson (2019). *Hekla volcano monitoring project*. Accessed from `https://en.vedur.is/media/vedurstofan-utgafa-2019/VI_2019_003_ICAO_final_web.pdf` on 13 June 2023. Icelandic Met Office.

Bayes, T. (1763). "LII. An essay towards solving a problem in the doctrine of chances. By the late Rev. Mr. Bayes, FRS communicated by Mr. Price, in a letter to John Canton, AMFR S". *Philosophical Transactions of the Royal So-*

ciety of London (53), pages 370–418. DOI: 10.1098/rstl.1763.0053.

Betancourt, M. (2017). "A conceptual introduction to Hamiltonian Monte Carlo". *arXiv:1701.02434 [stat.ME]*. DOI: 10.48550/arXiv.1701.02434.

Björnsson, H. and M. T. Guðmundsson (1993). "Variations in the thermal output of the subglacial Grímsvötn caldera, Iceland". *Geophysical Research Letters* 20(19), pages 2127–2130. DOI: 10.1029/93GL01887.

Böðvarsson, R. and B. Lund (2003). "The SIL seismological data acquisition system —As operated in Iceland and in Sweden—". *Methods and Applications of Signal Processing in Seismic Network Operations*. Berlin, Heidelberg: Springer Berlin Heidelberg, pages 131–148. ISBN: 978-3-540-47914-7. DOI: 10.1007/BFb0117700.

Böðvarsson, R., S. T. Rognvaldsson, S. S. Jakobsdottir, R. Slunga, and R. Stefansson (1996). "The SIL data acquisition and monitoring system". *Seismological Research Letters* 67(5), pages 35–46. DOI: 10.1785/gssrl.67.5.35.

Currenti, G., P. Jousset, R. Napoli, C. Krawczyk, and M. Weber (2021). "On the comparison of strain measurements from fibre optics with a dense seismometer array at Etna volcano (Italy)". *Solid Earth* 12(4), pages 993–1003. DOI: 10.5194/se-12-993-2021.

Daley, T. M., D. E. Miller, K. Dodds, P. Cook, and B. M. Freifeld (2016). "Field testing of modular borehole monitoring with simultaneous distributed acoustic sensing and geophone vertical seismic profiles at Citronelle, Alabama". *Geophysical Prospecting* 64 (5), pages 1318–1334. DOI: 10.1111/1365-2478.12324.

Daley, T. M., R. Pevzner, V. Shulakova, S. Kashikar, D. E. Miller, J. Goetz, and J. H. ans S. Lueth (2013). "Field testing of fiber-optic distributed acoustic sensing (DAS) for subsurface seismic monitoring". *The Leading Edge* 32 (6), pages 699–706. DOI: 10.1190/tle32060699.1.

Dou, S., N. Lindsey, A. M. Wagner, T. M. Daley, B. Freifeld, M. Robertson, J. Peterson, C. Ulrich, E. Martin, and J. B. Ajo-Franklin (2017). "Distributed Acoustic Sensing for seismic monitoring of the near surface: A traffic-noise interferometry study". *Scientific Reports* 7. 1162. DOI: 10.1038/s41598-017-11986-4.

Duane, S., A. D. Kennedy, B. J. Pendleton, and D. Roweth (1987). "Hybrid Monte Carlo". *Physics Letters B* 195 (2), pages 216–222. DOI: 10.1016/0370-2693(87)91197-X.

Fichtner, A. (2010). *Full Seismic Waveform Modelling and Inversion*. Springer, Heidelberg. DOI: 10.1007/978-3-642-15807-0.

– (2021). *Lecture Notes on Inverse Theory*. Cambridge Open Engage. DOI: 10.33774/coe-2021-qpq2j.

Fichtner, A., C. Hofstede, B. L. N. Kennett, N. F. Nymand, M. L. Lauritzen, D. Zigone, and O. Eisen (2023). "Fiber-optic airplane seismology on the Northeast Greenland Ice Stream". *The Seismic Record* 3 (2), pages 125–133. DOI: 10.1785/0320230004.

Fichtner, A. and S. Simute (2018). "Hamiltonian Monte Carlo inversion of seismic sources in complex media". *Journal of Geophysical Research: Solid Earth* 123 (4), pages 2984–2999. DOI: 10.1002/2017JB015249.

Fichtner, A., S. Klaasen, S. Thrastarson, Y. Çubuk-Sabuncu, P. Paitz, and K. Jónsdóttir (2022). "Fiber-optic observation of volcanic tremor through floating ice sheet resonance". *The Seismic Record* 2(3), pages 148–155. DOI: 10.1785/0320220010.

Flóvenz, Ó. G., R. Wang, G. P. Hersir, T. Dahm, S. Hainzl, M. Vassileva, V. Drouin, S. Heimann, M. P. Isken, E. Á. Gudnason, et al. (2022). "Cyclical geothermal unrest as a precursor to Iceland's 2021 Fagradalsfjall eruption". *Nature Geoscience* 15, pages 397–404. DOI: 10.1038/s41561-022-00930-5.

Gentili, S. and A. Michelini (2006). "Automatic picking of P and S phases using a neural tree". *Journal of Seismology* 10, pages 39–63. DOI: 10.1007/s10950-006-2296-6.

Global Volcanism Program (2011). "Report on Grimsvotn (Iceland)". *Bulletin of the Global Volcanism Network* 36(6). Edited by R. Wunderman. ISSN: 1050-4818. DOI: 10.5479/si.GVP.BGVN201106-373010.

Got, J.-L., A. Carrier, D. Marsan, F. Jouanne, K. Vogfjörd, and T. Villemin (2017). "An analysis of the nonlinear magma-edifice coupling at Grimsvötn volcano (Iceland)". *Journal of Geophysical Research: Solid Earth* 122(2), pages 826–843. DOI: 10.1002/2016JB012905.

Guðmundsson, M. T. and J. Milsom (1997). "Gravity and magnetic studies of the subglacial Grímsvötn volcano, Iceland: Implications for crustal and thermal structure". *Journal of Geophysical Research: Solid Earth* 102(B4), pages 7691–7704. DOI: 10.1029/96JB03808.

Gutenberg, B. (1956). "The energy of earthquakes". *Quarterly Journal of the Geological Society* 112(1-4), pages 1–14. DOI: 10.1144/GSL.JGS.1956.112.01-04.02.

Hartog, A. H. (2017). *An introduction to distributed optical fibre sensors*. CRC press. DOI: 10.1201/9781315119014.

Hreinsdotóttir, S., F. Sigmundsson, M. J. Roberts, H. Björnsson, R. Grapenthin, P. Arason, T. Árnadóttir, J. Hólmjárn, H. Geirsson, R. A. Bennett, et al. (2014). "Volcanic plume height correlated with magma-pressure change at Grímsvötn Volcano, Iceland". *Nature Geoscience* 7, pages 214–218. DOI: 10.1038/ngeo2044.

Hudson, T. S., A. F. Baird, J.-M. Kendall, S.-K. Kufner, A. M. Brisbourne, A. M. Smith, A. Butcher, A. Chalari, and A. Clarke (2021). "Distributed Acoustic Sensing (DAS) for natural microseismicity studies: A case study from Antarctica". *Journal of Geophysical Research: Solid Earth* 126(7). e2020JB021493. DOI: 10.1029/2020JB021493.

Igel, H. (2016). *Computational seismology: A practical introduction*. Oxford University Press. DOI: 10.1093/acprof:oso/9780198717409.001.0001.

Jousset, P., G. Currenti, B. Schwarz, A. Chalari, F. Tilmann, T. Reinsch, L. Zuccarello, E. Privitera, and C. M. Krawczyk (2022). "Fibre optic distributed acoustic sensing of volcanic events". *Nature Communications* 13. 1753. DOI: 10.1038/s41467-022-29184-w.

Jousset, P., T. Reinsch, T. Ryberg, H. Blanck, A. Clarke, R. Aghayev, G. P. Hersir, J. Henninges, M. Weber, and C. M. Krawczyk (2018). "Dynamic strain determination using fibre-optic cables allows imaging of seismological and structural features". *Nature Communications* 9. 2509. DOI: 10.1038/s41467-018-04860-y.

Klaasen, S. (2023). "Supplementary material to 'Subglacial volcano monitoring with fibre-optic sensing: Grímsvötn, Iceland'". *Zenodo*. DOI: 10.5281/ZENODO.8318425. [Dataset].

Klaasen, S., P. Paitz, N. Lindner, J. Dettmer, and A. Fichtner (2021). "Distributed acoustic sensing in volcano-glacial environments—Mount Meager, British Columbia". *Journal of Geophysical Research: Solid Earth* 126(11). e2021JB022358. DOI: 10.1029/2021JB022358.

Klaasen, S., S. Thrastarson, A. Fichtner, Y. Çubuk-Sabuncu, and K. Jónsdóttir (2022). "Sensing Iceland's Most Active Volcano with a "Buried Hair"". *Eos* 103. DOI: 10.1029/2022EO220007.

Komatitsch, D. and J. P. Vilotte (1998). "The spectral element method: an effective tool to simulate the seismic response of 2D and 3D geological structures". *Bulletin of the Seismological Society of America* 88 (2), pages 368–392. DOI: 10.1785/BSSA0880020368.

Lellouch, A., N. J. Lindsey, W. L. Ellsworth, and B. L. Biondi (2020). "Comparison between distributed acoustic sensing and geophones: Downhole microseismic monitoring of the FORGE geothermal experiment". *Seismological Research Letters* 91(6), pages 3256–3268. DOI: 10.1785/0220200149.

Lindsey, N. J. and E. Martin (2021). "Fiber-optic seismology". *Annual Review of Earth and Planetary Sciences* 49, pages 309–336. DOI: 10.1146/annurev-earth-072420-065213.

Lindsey, N. J., E. R. Martin, D. S. Dreger, B. Freifeld, S. Cole, S. R. James, B. L. Biondi, and J. B. Ajo-Franklin (2017). "Fiber-optic network observations of earthquake wavefields". *Geophysical Research Letters* 44(23), pages 11792–11799. DOI: 10.1002/2017GL075722.

Lindsey, N. J., H. Rademacher, and J. B. Ajo-Franklin (2020). "On the broadband instrument response of fiber-optic DAS arrays". *Journal of Geophysical Research: Solid Earth* 125(2). e2019JB018145. DOI: 10.1029/2019JB018145.

Lior, I., A. Sladen, D. Mercerat, J.-P. Ampuero, D. Rivet, and S. Sambolian (2021). "Strain to ground motion conversion of distributed acoustic sensing data for earthquake magnitude and stress drop determination". *Solid Earth* 12, pages 1421–1442. DOI: 10.5194/se-12-1421-2021.

Martin, E. R., C. M. Castillo, S. Cole, P. S. Sawasdee, S. Yuan, R. Clapp, M. Karrenbach, and B. L. Biondi (2017). "Seismic monitoring leveraging existing telecom infrastructure at the SDASA: Active, passive, and ambient-noise analysis". *The Leading Edge* 36 (12), pages 962–1044. DOI: 10.1190/tle36121025.1.

Masfara, L. O. M., T. Cullison, and C. Weemstra (2022). "An efficient probabilistic workflow for estimating induced earthquake parameters in 3D heterogeneous media". *Solid Earth* 13, pages 1309–1325. DOI: 10.5194/se-13-1309-2022.

Mateeva, A., J. Lopez, H. Potters, J. Mestayer, B. Cox, D. Kiyashchenko, P. Wills, S. Grandi, K. Hornman, B. Kuvshinov, et al. (2014). "Distributed acoustic sensing for reservoir monitoring with vertical seismic profiling". *Geophysical Prospecting* 62(4), pages 679–692. DOI: 10.1111/1365-2478.12116.

Neal, R. (2012). "MCMC Using Hamiltonian Dynamics". *Handbook of Markov Chain Monte Carlo*. DOI: 10.1201/b10905-7.

Paitz, P., P. Edme, D. Gräff, F. Walter, J. Doetsch, A. Chalari, C. Schmelzbach, and A. Fichtner (2021). "Empirical investigations of the instrument response for distributed acoustic sensing (DAS) across 17 octaves". *Bulletin of the Seismological Society of America* 111(1), pages 1–10. DOI: 10.1785/0120200185.

Porter, C., P. Morin, I. Howat, M.-J. Noh, B. Bates, K. Peterman, S. Keesey, M. Schlenk, J. Gardiner, K. Tomko, M. Willis, C. Kelleher, M. Cloutier, E. Husby, S. Foga, H. Nakamura, M. Platson, M. Wethington, C. Williamson, G. Bauer, J. Enos, G. Arnold, W. Kramer, P. Becker, A. Doshi, C. D'Souza, P. Cummens, F. Laurier, and M. Bojesen (2018). *ArcticDEM, Version 3*. Type: dataset. DOI: 10.7910/DVN/OHHUKH.

Reynolds, H. I., M. T. Guðmundsson, T. Högnadóttir, and F. Pálsson (2018). "Thermal power of Grímsvötn, Iceland, from 1998 to 2016: Quantifying the effects of volcanic activity and geothermal anomalies". *Journal of Volcanology and Geothermal Research* 358, pages 184–193. DOI: 10.1016/j.jvolgeores.2018.04.019.

Roberts, N. S., A. F. Bell, and I. G. Main (2015). "Are volcanic seismic b-values high, and if so when?" *Journal of Volcanology and Geothermal Research* 308, pages 127–141. DOI: 10.1016/j.jvolgeores.2015.10.021.

Saragiotis, C. D., L. J. Hadjileontiadis, and S. M. Panas (2002). "PAI-S/K: a robust automatic seismic P phase arrival identification scheme". *IEEE Transactions on Geoscience and Remote Sensing* 40 (6), pages 1395–1404. DOI: 10.1109/TGRS.2002.800438.

Simute, S., C. Boehm, L. Krischer, A. Gokhberg, M. Vallée, and A. Fichtner (2023). "Bayesian seismic source inversion with a 3-D Earth model for the Japanese islands". *Journal of Geophysical Research: Solid Earth* 128 (1). e2022JB024231. DOI: 10.1029/2022jb024231.

Sleeman, R. and T. van Eck (1999). "Robust automatic P-phase picking: an on-line implementation in the analysis of broadband seismogram recordings". *Physics of the Earth and Planetary Interiors* 113 (1-4), pages 265–275. DOI: 10.1016/S0031-9201(99)00007-2.

Slunga, R. (1981). "Earthquake source mechanism determination by use of body-wave amplitudes—an application to Swedish earthquakes". *Bulletin of the Seismological Society of America* 71(1), pages 25–35. DOI: 10.1785/BSSA0710010025.

Stefánsson, R., R. Böðvarsson, R. Slunga, P. Einarsson, S. Jakobsdóttir, H. Bungum, S. Gregersen, J. Havskov, J. Hjelme, and H. Korhonen (1993). "Earthquake prediction research in the South Iceland Seismic Zone and the SIL project". *Bulletin of the Seismological Society of America* 83(3), pages 696–716. DOI: 10.1785/BSSA0830030696.

Tarantola, A. (2005). *Inverse problem theory and methods for model parameter estimation, 2nd edition.* Society for Industrial and Applied Mathematics, Philadephia. DOI: 10.1137/1.9780898717921.

Thelen, W. A., R. S. Matoza, and A. J. Hotovec-Ellis (2022). "Trends in volcano seismology: 2010 to 2020 and beyond". *Bulletin of Volcanology* 84. 26. DOI: 10.1007/s00445-022-01530-2.

Thordarson, T. and S. Self (1993). "The Laki (Skaftár fires) and Grímsvötn eruptions in 1783–1785". *Bulletin of Volcanology* 55, pages 233–263. DOI: 10.1007/BF00624353.

Thordarson, T. and S. Self (2003). "Atmospheric and environmental effects of the 1783–1784 Laki eruption: A review and reassessment". *Journal of Geophysical Research: Atmospheres* 108(D1), AAC 7-1–29. DOI: 10.1029/2001JD002042.

Thrastarson, S., R. Torfason, S. Klaasen, P. Paitz, Y. Çubuk-Sabuncu, K. Jónsdóttir, and A. Fichtner (2021). "Detecting Seismic Events with Computer Vision: Applications for Fiber-Optic Sensing". *ESS Open Archive*. DOI: 10.1002/essoar.10509693.1.

Walter, F., D. Gräff, F. Lindner, P. Paitz, M. Köpfli, M. Chmiel, and A. Fichtner (2020). "Distributed acoustic sensing of microseismic sources and wave propagation in glaciated terrain". *Nature Communications* 11. 2436. DOI: 10.1038/s41467-020-15824-6.

Wang, H. F., X. Zeng, D. E. Miller, D. Fratta, K. L. Feigl, C. H. Thurber, and R. J. Mellors (2018). "Ground motion response to an ML 4.3 earthquake using co-located distributed acoustic sensing and seismometer arrays". *Geophysical Journal International* 213(3), pages 2020–2036. DOI: 10.1093/gji/ggy102.

Zhu, W. and G. Beroza (2019). "PhaseNet: a deep-neural-network-based seismic arrival time picking method". *Geophys. J. Int.* 216, pages 261–273. DOI: 10.1093/gji/ggy423.

Zunino, A., L. Gebraad, A. Ghirotto, and A. Fichtner (2023). "HMCLab: a framework for solving diverse geophysical inverse problems using the Hamiltonian Monte Carlo method". *arXiv*. DOI: 10.48550/arXiv.2303.10047.